NOVEL & RAPID PROCESSING OF UAS IMAGERY FOR TARGETED CYANOBACTERIAL HARMFUL ALGAL BLOOM SAMPLING

Authors

Reckling, William[1,2*]; Levine, Jay[2]; Sánchez-Gallego, Joel J.[2,3]; Huang, Hwa[2]; Walton, Troy[4]; Plaas, Haley E.[4,5]; Popendorf, Kimberly J.[6]; Paerl, Ryan W.[2]

Affiliations

1 Center for Geospatial Analytics, North Carolina State University, Raleigh, NC, USA

2 Marine, Earth and Atmospheric Sciences, North Carolina State University, Raleigh, NC, USA

3 Coiba Scientific Station, City of Knowledge, Clayton, Panama

4 Environmental Science and Engineering, University of North Carolina, Chapel Hill, NC, USA

5 Institute of Marine Sciences, University of North Carolina, Morehead City, NC, USA

6 Rosenstiel School of Marine, Atmospheric, and Earth Science, University of Miami, Miami, Florida, USA

*Corresponding Author

Author Contributions

William Reckling: Conceptualization, Data curation, Formal analysis, Methodology, Software, Validation; Visualization, Roles/Writing - original draft, Writing - review & editing. **Jay Levine:** Writing - review & editing. **Joel Sánchez:** Investigation, Formal analysis. **Hwa Huang:** Investigation, Formal analysis. **Troy Walton:** Investigation, Methodology, Resources. **Haley Plaas:** Investigation, Formal analysis, Methodology. **Kimberly Popendorf:** Investigation, Formal analysis, Methodology. **Ryan Paerl:** Investigation, Formal analysis, Methodology, Validation; Visualization, Writing - review & editing.

Abstract

Unmanned aerial systems (UAS) are an efficient way to monitor and sample algal biomass including cyanobacterial harmful algal blooms (CyanoHABs). However, conventional methods to create a UAS orthophoto of homogeneous water surfaces often produce a patchy,

smoothed, or spatially inaccurate output. In this study, we developed a novel method to interpolate a spectral index from a central pixel in individual aerial photos to rapidly map the distribution of algal biomass. The results of our interpolation method align well with orthomosaic-derived indices and UAS-collected water samples analyzed in the laboratory, affirming the reliability of our approach. This alignment further strengthens our ability to monitor, detect, and alert the public of algal growth via rapid system-wide assessment as well as targeted sampling of low and high-biomass regions. Last, we demonstrate how simple UAS sampling associated with imagery analyses enables genetic- and microscopy-based assessment of collected algal biomass as well as cyanotoxin concentrations.

Keywords: Unmanned aerial system; UAS; drone; algal bloom; CyanoHABs; orthomosaic; spectral index; water sampling

1. Introduction

Cyanobacteria (blue-green algae) and eukaryotic phytoplankton are photoautotrophic organisms that occur naturally in aquatic environments worldwide (1–4). Cyanobacterial algal blooms occur when increased nutrient availability enables an excess of biomass to accumulate. The health of aquatic fauna and ecosystems as well as humans proximal to aquatic systems are at risk during blooms that can produce toxins, alter water quality (pH, dissolved oxygen - during decay), air quality (5), and accumulate into thick surface scums (5,6). Cyanotoxins (e.g., microcystin, anatoxins, saxitoxins) produced by the cyanobacteria during these cyanobacterial harmful algal blooms (CyanoHABs) can impede human water use (e.g., irrigation, fishing, drinking, and recreation) enter the aquatic food web and food stocks consumed by humans (5,7,8). Additionally, unsightly or odorous cyanobacterial blooms may negatively affect tourism, property value (9), and human perception of surface water quality (6). Nutrient over-enrichment in aquatic systems and climate change are accelerating the size, intensity, and frequency of CyanoHABs (10–12).

The potential rapid growth, migration, and persistence of cyanobacteria can be challenging to monitor, manage, and eliminate (6,13,14).On-site water sampling (grab, scoop, and photic) and remote sensing (UAS, and satellite) are established algal and cyanobacterial monitoring methods (15,16). However, field sampling and surveys by boat are limited to accessible locations and can disrupt and disperse surface blooms (17,18). World Health Organization (WHO) guidelines recommend adaptive monitoring of CyanoHABs when sampling is increased as cyanobacteria levels increase (19). Also, to identify areas with the greatest public exposure risk, sampling is often performed in areas with concentrated blooms or near public beaches, boat ramps, or drinking water intakes (16). While budgetarily pragmatic, single-site sampling from docks or land may not be representative of the spatial distribution of biological and chemical conditions during a large-scale bloom.

Water sampling using UAS overcomes some limitations of traditional water sampling methods. UAS has have been successfully fitted with pumps for onboard collection (17,18,20,21), and with sampling devices suspended from the aircraft (18,22–25). In most cases, measurements obtained from samples collected by UAS align closely with those obtained through traditional sampling methods (17,20,21,25,26). However, sometimes the results obtained by UAS differ from surface collection methods because of disruption to the water surface during sample collection (22,27). Additionally, UAS sampling devices can be expensive (17,26), and sampling can be limited by flight time, payload weight, or volume (27). To increase collection efficiency, some studies have used preplanning with navigational system waypoints that optimize data (17,24,26,28).

Visible surface scums can be an indicator of an algal bloom (6) and are discernible in remotely sensed satellite or UAS imagery (29). Algal blooms can be detected in the imagery using the reflectance and absorbance characteristics of different electromagnetic spectrum wavelengths (29). A spectral index can further highlight features by combining the reflectance

values from two or more bands. Although many spectral indices target terrestrial vegetation, several have been developed specifically for algal blooms. The Cyanobacteria Index (CI) or Normalized Difference Chlorophyll Index (NDCI) detect chlorophyll by comparing reflection values in the near-infrared range and absorption in the red and blue bands (30–32). The Cyanobacteria Assessment Network (CyAN) project, established to detect algal blooms in U.S. freshwater systems, uses the CI to estimate cyanobacteria concentrations across the United States from the MERIS and Sentinel-3 satellites with a spatial resolution of 300 m (33). The NDCI has been used to estimate Chlorophyll a (Chl-a) concentrations, as a proxy for biomass, from the Sentinel-2 satellites with a spatial resolution of 10 m (30). The NDCI has also been applied to Sentinel-3 and Landsat-8 imagery with 300 m and 30 m resolutions, respectively (30). However, satellites can have days-long satellite revisit times, can be obscured by cloud cover, and coarser spatial resolutions do not allow for the identification of localized or transient HAB events (34,35). Additionally, while many datasets are freely available from government agencies, higher spatial and temporal resolution commercial datasets come with substantial cost (35,36). Relevant commercial satellite resolutions range from 0.3 to 3 m, costing $0.012 - $0.275 per hectare (36).

Remote sensing CyanoHABs with UAS is relatively cost-efficient, and UAS systems can be easily deployed by field personnel (35,37). While it is possible to use a drone with red edge or near-infrared (NIR) detection capabilities to calculate algae-specific indices (37,38), several indices have been demonstrated to work with common and less expensive visible spectrum red, green, and blue (RGB) UAS sensors (Table 1). These RGB vegetation indices are good proxies for algorithms that include the NIR to detect algal blooms or chlorophyll-a (37,39,40).

Table 1. Visible spectrum indices used to identify algal blooms or chlorophyll-a in water. R, G, and B represent red, green, and blue bands.

Index	Formula	Reference
ExGI, 2G_Rbi	ExGI = (2 * G) - (R + B)	(41–44)

GCC, Channel G%	GCC = G / (R + G + B)	(42,43,45)
NGRDI, GRVI, SNDVI	NGRDI = (G - R) / (G + R)	(44,46–48)
NGBDI	NGBDI = (G - B) / (G + B)	(44)
VARI	VARI = (G - R) / (G + R - B)	(49)
VDVI, GLI	VDVI = ((2*G) - R - B) / ((2 * G) + R + B)	(44,50,51)
VWRI	VWRI =(G - B - R) / (G + B + R)	(52)

While UAS sampling and data collection has become more commonplace, their operation is limited by regulations, battery time, and payload capacity (17,26,27,53). Creating geospatially accurate orthomosaics from aerial photographs is also time-consuming (54). Aerial imagery is subject to systematic error, inherent distortions, and displacements caused by topography, aircraft motion, and lens characteristics, which require correction and calibration before and during processing (55–58). Additionally, the homogenous appearance of water makes it difficult to extract unique key points from each image in structure from motion software (SfM) workflows (40,59). The combination of systematic and key point matching errors make it challenging to create a complete or accurate orthomosaic over water (35,37,38,53,60,61) and may result in a noisy and distorted output (59,61). While results can be improved by using ground control points (GCPs) (55,58), a real-time kinematic global navigation satellite system (RTK GNSS), capturing a continuous shoreline, or adding markers in the water (55,62), orthomosaic generation over water remains difficult. Recent efforts to mosaic images have succeeded in making a spatially accurate representation, but the patchy nature of a mosaic makes calculating a usable spectral index difficult (63). The authors of this paper initially employed a similar method but ultimately shifted to the approach detailed in this study.

Targeted UAS sampling is an efficient way to monitor and sample algal growth and CyanoHABs. Since conventional methods to create a UAS orthomosaic of homogeneous water surfaces often result in a patchy, smoothed, or spatially inaccurate output [24,50], we developed a novel method to rapidly map the distribution of algal biomass from UAS images to guide efficient collection of samples using UAS. We applied this method using UAS-collected data at

Waterville Lake in western North Carolina and the Chowan River in eastern North Carolina – two regions often impacted by CyanoHABs (5,64–67). We interpolated a spectral index from a central pixel in the individual aerial photos to represent and then target specific bloom areas for sample collection.

2. Methods

We developed a methodology for flying a low-cost drone to efficiently target collection of water samples, and imagery, and rapidly create a map representing areas with high concentrations of CyanoHABs. The map was then used to guide water sample collection for downstream laboratory analysis (Figure 1).

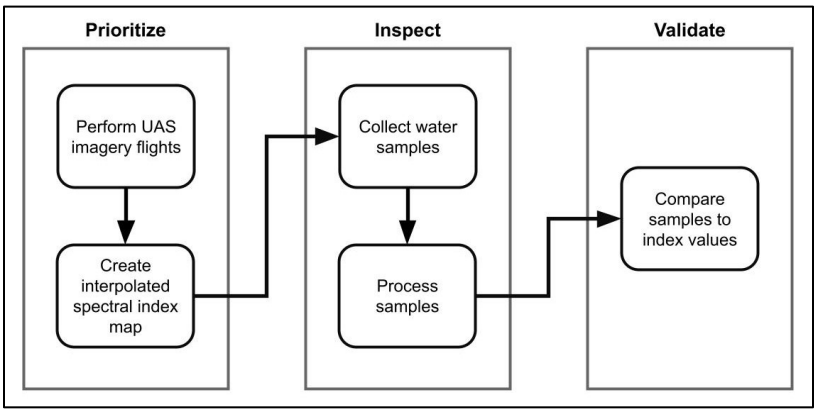

Figure 1. Conceptual diagram of the methodological workflow used for algal bloom detection and downstream analyses.

2.1 Study locations

The proposed methodology was tested at Waterville Lake and the Chowan River, two systems with distinct characteristics that have documented recurring CyanoHABs (5,64–67). Site A was Waterville Lake (35°41'41.1"N, 83°03'00.1"W), situated in the Blue Ridge mountains of Western North Carolina at 688m elevation. Waterville Lake is a 300-acre reservoir created in the 1930s with the construction of the 55-meter-tall Walters hydroelectric dam on the Pigeon River (68). Directly upstream from the dam are a landfill and an active papermill from the early 1900s

that released wastewater containing toxic chemicals such as dioxins, furan, and chloroform into the Pigeon River for almost 80 years (69). There is a public canoe portage site and private boat ramp, but a locked gate controls access to the dam and immediate vicinity. Entry to the site was facilitated by utility company personnel. Site B was the Chowan River, an 80-kilometer river in eastern North Carolina that flows into the Albemarle Sound. The field sampling location is located on the east bank of the Chowan River (36°12'43.4"N, 76°42'51.4"W) at a private dock in the rural Arrowhead Beach community. The Chowan River is 2600 meters across in this location. The Chowan River basin receives nutrients from municipal and industrial treatment processes and runoff from 959 agricultural farms, 40 swine, 132 poultry, and 440 timber harvesting operations (70).

2.2 UAS imagery acquisition and processing

To assess the presence of CyanoHABs, we deployed UASs at Waterville Lake and the Chowan River to collect imagery and surface water samples. The collected aerial photos were used to create orthomosaics and interpolated raster maps that we compared to each other and extracted chlorophyll-a from water samples.

2.2.1 Imagery collection

The UAS imagery collection flight at Waterville Lake (Site A) was conducted on October 28th, 2019, at 10:48 am from the gravel parking lot adjacent to Walters Dam, with a flight duration of approximately 10 minutes. Eighty-three photos were collected with a Parrot Anafi Thermal quadcopter equipped with a Sony 26 mm focal length, 21-megapixel RGB camera, and FLIR Lepton 3.5 microbolometer thermal sensor (71). The Anafi uses a four-constellation U-BLOX UBX-M8030 Global Navigation Satellite System (GNSS) receiver with a 2m horizontal position accuracy (72). The flight was autonomously flown at 121 meters above ground elevation in a crosshatch flight pattern, with 70% front and side overlap, and 90 degrees nadir camera gimbal angle using the Pix4Dcapture application (73). The sky was cloudy with a low ceiling after light rain the previous day into the morning.

The UAS imagery collection flight at Chowan River (Site B) was performed on July 21st, 2020, at 8:34 am from a private dock with a flight duration of approximately 30 minutes. Four hundred eighty-six photos were collected with a DJI Phantom 4 Pro quadcopter with a 24 mm focal length and 20-megapixel RGB sensor (74). The manufacturer, DJI , has not published the positional accuracy for the Phantom 4 Pro dual constellation GNSS receiver. The flight was autonomously flown at 100 meters above ground elevation in a linear track flight pattern, with 30% front and side overlap, and 90 degrees nadir camera gimbal angle using the DroneDeploy flight app (75). A polygon flight area of 300 acres was selected because the flight planning software estimated a 20-minute flight time, the capacity of one battery. An error in the onboard mission plan caused the UAS to collect double the number of photos, resulting in a battery swap midway through the flight. Once the UAS was airborne again, the glitch was resolved, and the UAS collected at the preplanned photo interval. Although the camera issue was noticed early in the flight, the flight was not restarted due to the incoming, spotty cloud cover, which would have affected the photos.

2.2.2 Spectral indices from orthomosaics

The acquired RGB aerial photography was processed in Agisoft Metashape 1.7.5 (76) with the highest quality and accuracy settings with mild depth filtering to eliminate noise in the point cloud (77). Orthomosaics were generated by rectifying the images to digital surface models created from the point clouds. The Normalized Green Blue Difference Index (NGBDI) and the Normalized Green Red Difference Index (NGRDI) were derived from the UAS orthomosaics in ArcGIS Pro 3.0.2 (78) with the same ground resolution as the original orthomosaics. The NGBDI and NGRDI indices contrast the green portion of the spectrum against the red or blue bands. The NGBDI is represented as (G-B)/(G+B), and the NGRDI is represented as (G-R)/(G+R) where G is the green band, B is the blue band, and R is the red band (44,48). We selected these two indices because they have previously outperformed other visible spectrum indices at distinguishing chlorophyll-a. They have also performed well in identifying algal blooms (37,39,41,79,80). A map algebra function was used to convert the orthomosaic pixel values into rasters representing each index. The spectral index rasters were masked with a

shoreline boundary polygon modified from National Hydrology Dataset (NHD) water areas (81).

2.2.3 Spectral indices from interpolation

Orthomosaic creation can be time-consuming and computationally intensive, and generating a complete orthomosaic over water is often difficult. We created an approximate spectral index map from drone images to guide sampling efforts. We used Python and the Pillow (82), gpsphoto (83), and ArcPy (78) libraries to derive an interpolated map representing spectral index values from the UAS aerial photos. First, we extracted the latitude, longitude, and red, green, and blue (RGB) digital number (DN) values for the central pixel (1 cell) and the surrounding 9 (3x3 cells) and 25 (5x5 cells) pixels in each aerial photo (Figure 2). The central pixel represents the location directly beneath the UAS at the latitude and longitude where the photo was taken and has the lowest radial lens distortion, which radiates from the center of an image (56,57). A pixel from an image at the studied altitudes, and camera characteristics, has a ground resolution of approximately 3 cm. The 9 and 25 cell window sizes were selected to evaluate variance from the central pixel caused by radial distortion, sun glint, or ripples. These windows were large enough to assess if there was a deviation from the central cell values but small enough to avoid falling outside of a ripple, band of dense CyanoHAB pigmentation, or interacting with shore features. The RGB values for the central (1 cell), 9, and 25 cell RGB values were used to calculate NGBDI and NGRDI spectral indices, which were averaged and joined to points created from coordinates representing each photo location. Inverse distance weighting (IDW) surface interpolation with barriers was used to generate raster maps from the index values associated with each photo point. A resolution of approximately 1 m was chosen for the interpolated map as a practical tradeoff between processing time and level of detail. To arrive at this conclusion, we examined five resolutions, namely 0.1 m, 0.25 m, 0.5 m, 1 m, and 5 m. The IDW with barrier allowed us to limit the interpolation to within the extent of the shoreline boundary polygon created from a combination of NHD water areas and a convex hull boundary created from the photo points. This polygon area contained the interpolation to areas over water and within the nadir photo points.

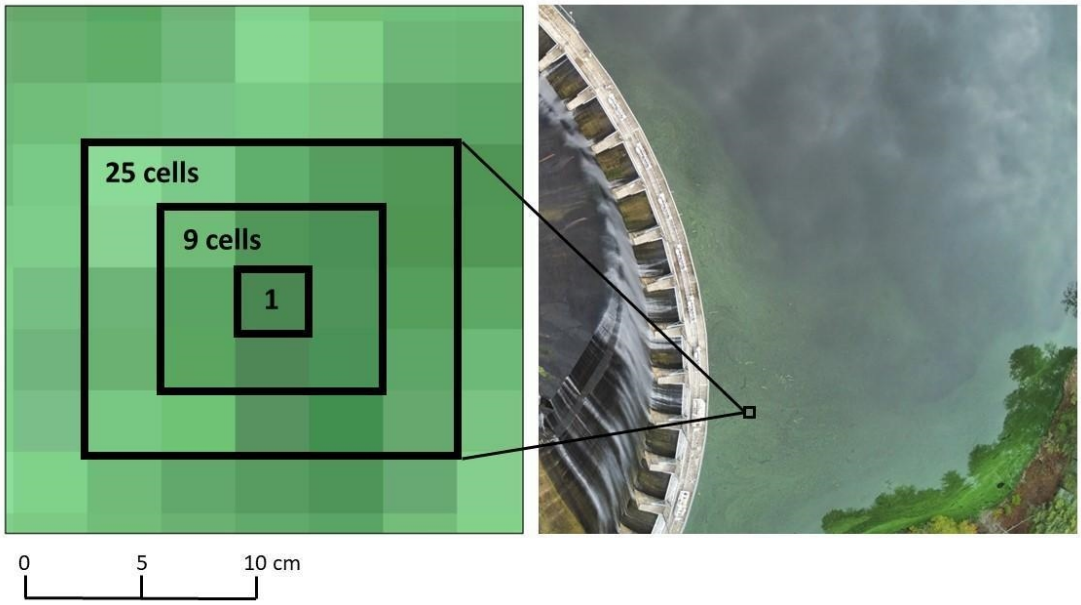

Figure 2. Central pixel (1 cell), 9 cell and 25 cell windows used to average spectral indices.

2.3 Water sample acquisition and processing

2.3.1 UAS sampling

Several types of sampling brackets have been used to sample water from UAS (22,23,27). Our UAS sampling rig design evolved as we learned from field testing. Each sampling rig included a sampling bracket suspended from the UAS by one or two lines from a Parrot Anafi or DJI Phantom 4 Pro quadcopter. Initially, we collected samples using a 3D-printed bracket holding a single 50 ml Falcon tube suspended from the UAS (Figure 3). To increase water carrying capacity, we fabricated a bracket for two 50 ml Falcon tubes out of an aluminum plate. The bracket's weight caused the tubes to invert, preventing water samples collection. Finally, we settled on a design with holes for two 50 ml Falcon tubes made from "plastic canvas" vinyl material available at any craft store. Each plastic canvas bracket costs less than 10 cents to make with scissors, is lightweight, and is semi-submersible, allowing the sampling tubes to fill with water (Figure 3). In early flight videos we observed surface water disturbance caused by propellor thrust, resulting in dispersion of the algal surface bloom. Therefore, we suspended the bracket at different lengths and observed that a length of 6 m did not disperse the bloom or impede the UAS flight and sampling. We tested several types of fishing line, but ultimately, a

neon green braided fishing line was chosen for its enhanced visibility and reduced tangling. The additional weight/rigidity minimizes the chance of the line being pulled into the props. Small plastic carabiners were attached to each end of the line to allow for the sampling bracket to be quickly changed between sampling flights.

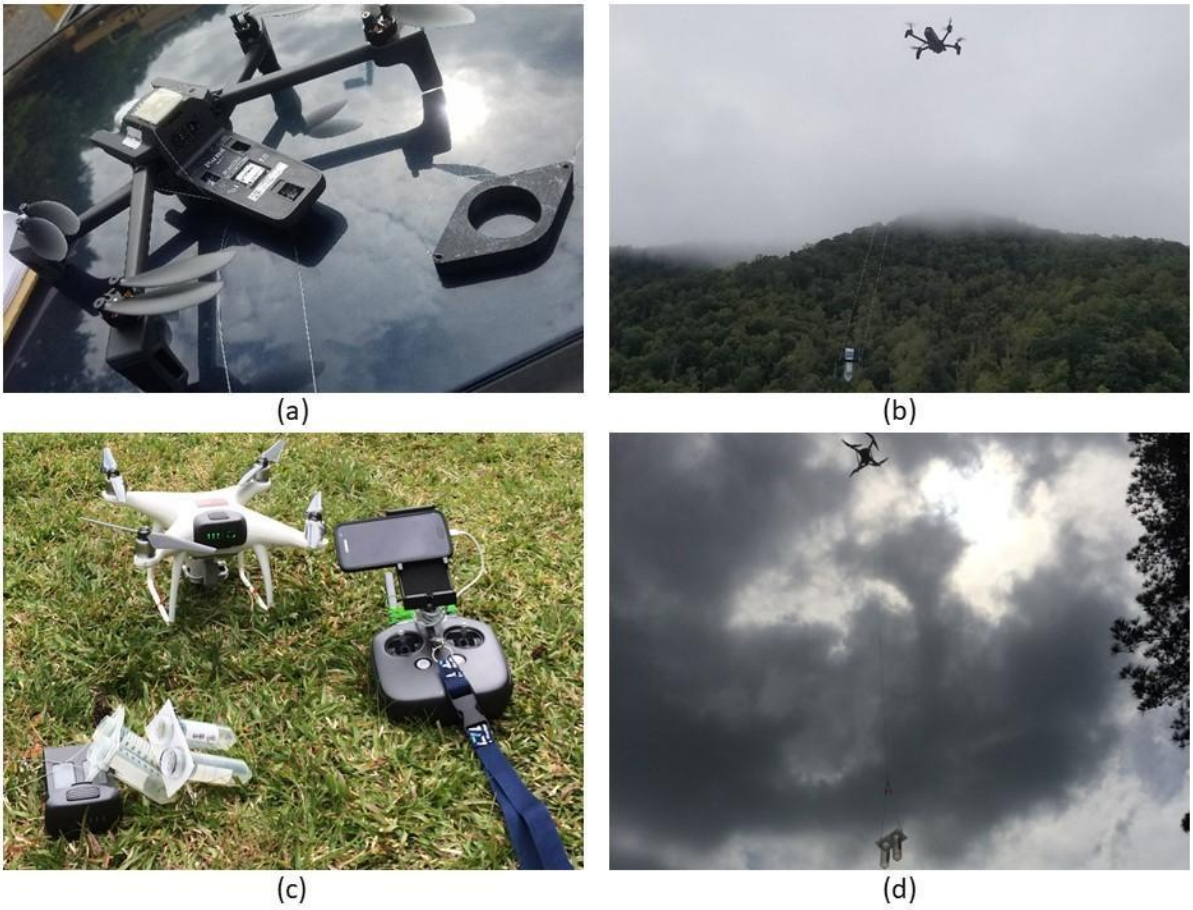

Figure 3. (a) Parrot Anfi Thermal UAS and 3D printed water sampling bracket, (b) carrying a 50ml tube of water at Site A, (c) DJI Phantom 4 Pro UAS and fabric mesh sampling brackets, (d) carrying dual 50ml tubes at Site B.

At Site A, the UAS was manually flown to four sampling locations with the Parrot FreeFlight 6 application (84). The samples were collected beginning at 10:03 am. At each site, a nadir photograph was taken to record the sampling location coordinates in the photograph's

Exif header. The live video feed was used to lower a 3Dprinted bracket holding a 50ml Falcon tube suspended by two 2m monofilament fishing lines into the water (Figure 3). Once filled, the UAS was flown back to the starting location, where the sample tubes were removed from the bracket, capped, and stored in a cooler. The samples were collected at four locations around the perimeter of the flight area (Figure 4). As a part of a larger pilot project to test UAS sampling, an additional seven samples were collected by UAS an hour before and two hours after the flight and were not included in the imagery analysis. Each sample took approximately three minutes to collect with the UAS. The samples were transported on ice in a cooler back to North Carolina State University for analysis.

At Site B, the UAS was manually flown to four sampling locations with the DJI Go application (85). The samples were collected beginning at 9:42 am. At each site, a nadir photograph was taken to record the sampling location coordinates in the photograph's Exif header. Visual observation and the live video feed were used to lower two 50 ml Falcon tubes in a fabric mesh bracket, suspended by two 6m braided fishing lines, into the water (Figure 3). Once filled, the UAS was flown back to the starting location, where the sample tubes were removed from the bracket, capped, stored in a cooler with ice, and replaced with empty tubes. The samples were collected at four locations starting at the dock, 100 m perpendicular to the shore, and 300 m parallel to the shore upstream and downstream from the dock (Figure 5). Each sample took approximately two minutes to collect with the UAS. The samples were transported on ice in a cooler back to North Carolina State University for analysis.

2.3.2 Laboratory water sample analysis

For Site A, collected surface water was processed for multiple analyses, including: *in-vivo* Chl-a fluorescence, flow cytometry (FCM) based counts of small phytoplankton (86), qualitative assessment of sample by light microscopy (Nikon Eclipse Ts2R), particulate microcystin concentrations (5,87), and DNA extraction from biomass for PCR detection microcystin-producing cyanobacteria. Collected surface water for FCM was prefiltered through 40 μm Nitex mesh to avoid clogging during analysis, fixed with glutaraldehyde (0.25% final conc.), and placed in the dark for 15 minutes before storage at -80°C. Thawed FCM samples

were analyzed using a dual laser (blue (488 nm), red (600 nm)) Guava EasyCyte HT (Millipore) flow cytometer. Events were recorded based on red fluorescence from Chl-a possessing cells excited by the blue excitation laser. Initial tests were completed to analyze the background noise and potential coincidence, which can impact counting. *Microcystis*-like cells were identified based on autofluorescence from blue and red laser excitation (88), as well as their relatively larger forward scatter compared to other small phytoplankton (*Synechococcus*-like and picoeukaryotic phytoplankton cells), and enumerated using GuavaSoft (Millipore). Spherical reference beads of known diameter (0.5 – 16.5 μm; Spherotech) were used to obtain an empirical relationship between median FSC (x) and bead diameter in micrometers (y), y = 1.4699e0.0002x; R2 = 0.91 (Figure A2), and estimate the diameter of cells based on FSC. *In-vivo* Chl-a fluorescence (indicator of phytoplankton biomass) in surface water samples was determined using an AquaFluor handheld fluorometer (Turner Designs). Whole water samples were also surveyed for abundant phytoplankton and imaged using a Nikon TS2R inverted microscope under white light. For DNA extraction, surface water was vacuum (<10 in. Hg) filtered through 25 mm SUPOR (Pall) 0.2 μm pore-sized filters, and filters plus biomass were stored at -80°C. DNA was extracted from biomass on filters using the Qiagen PowerWater kit with the following modifications: 1) addition of sapphire disruption beads to sterile 2mL screw cap tubes, and 2) performing 5 min of bead beating at 2.5 x 1000 oscillations per minute using a BioSpec Mini 16 beadbeater. Obtained DNA was quantified using a Qubit and Picogreen Kit (Invitrogen). Primers targeting the V4-5 region of cyanobacterial 16S rRNA genes (89) as well as a partial region of the microcystin synthase A gene (*mcyA*) (90) were used in PCR amplification. Apex Red 2.0x Taq Mastermix (Apex Bioresearch Products) was used in all PCR reactions, following the protocols published for each primer set. Equal volumes or quantities of extracted DNA were added to respective PCR reactions for intercomparison between samples. Internal positive controls (*Microcystis aeruginosa* UTEX 2385 DNA) confirmed no inhibition of PCR amplification.

For particulate microcystin quantification, surface water was gently filtered by syringe and loaded Swinlock (Whatman) through glass fiber filters (GF/F; Whatman) until dry and

stored at -20°C until use. Due to limited sample volume, single GFF filters with biomass were collected from each station. Samples were shipped on dry ice to the Popendorf lab at the University of Miami for extraction and identification of eight microcystin congeners using targeted liquid chromatography-tandem mass spectrometry (LC-MS/MS) (5,87). MCs were quantified via concentration curves generated from commercially available standards; limits of detection were specific to each congener (Table A2). Explicit extraction protocols and instrument settings are detailed in Gaston et al., 2021 (87).

At Site B collected water was filtered through GF/F filters by vacuum (<10 in. Hg). Chl-a was extracted and quantified from biomass on GF/F filters using the non-acidification 90% acetone method [81] and a standard curve calibrated Trilogy fluorometer (Turner Designs).

2.4 Relationship between the spectral indices, resolution, and algae biomass

We investigated the relationship between the spectral indexes derived from the orthomosaic, interpolated map, and *in-situ* Chl-a measurements. First, to compare spectral index values derived from the orthomosaics and the interpolation method, we used QGIS (91)to resample the orthomosaics to 1 m resolution with bilinear interpolation to match the interpolated maps. Next, we generated 100 random points within the combined photo point and water area boundary. The spectral index values were sampled at each point and exported to a table. We removed null values (patchy areas in the orthomosaics). Then we performed the Spearman correlation in Python NumPy (92) to evaluate the relationships between the spectral index values derived from the orthomosaics and the interpolation method. We also performed Spearman coefficient correlation analysis to compare the central pixel (1 cell) values to the 9, and 25-cell averages. A P-value of < -0.05 was considered statistically significant. Next, we created sampling location points with the ImportPhotos plugin (93) from the photograph coordinates to evaluate the correlation between the orthomosaic derived and interpolated index values and *in-situ* chlorophyll-a measurements. We joined the *in-situ* Chl-a values to an exported table and used NumPy to apply a linear regression for each index to compare the linearities by the adjusted coefficient of determination (r^2) (39). Normality of the residuals and

the homoscedasticity of the models were verified using the Shapiro-Wilk and Breusch-Pagan tests available in SciPy (94) at the 95% confidence interval.

3. Results

3.1 Orthomosaics and derived indices

It took 10 and 114 minutes to process the imagery from the Site A and B flight datasets, respectively. Fifty-three out of 83 photos from Site A and 116 out of 486 photos from Site B were aligned during the alignment step. The UAV camera x,y,z (latitude, longitude, elevation) location error estimates were lower along the shore areas and increased with distance away from discernible features (Figure A1). Orthomosaics and spectral index rasters were produced with ground resolutions of 3.76 and 2.58 cm/px for Sites A and B, respectively (Figures 5, 6 and 7). The resampled indices were generated with a 1 m resolution. Even without ground control points, the orthomosaics were well aligned to shore features in existing georeferenced North Carolina imagery (95). At Site A, the high-resolution orthomosaic and derived indices provided sufficient detail for visually identifying areas with higher biomass. At Site B, the orthomosaic was only generated in an area along the shore due to image alignment issues in the photogrammetry process.

3.2 Interpolated indices

The central pixel in the unrectified aerial photos from Site A and B represented a resolution of approximately 3 cm/px. Processing time for the Site A aerial photos was less than 30 seconds and less than 60 seconds for Site B, an improvement of 20x and 100x over the traditional orthomosaic method. The NGBDI values ranged from -0.17 to 0.16 at Site A and -0.27 and 0.06 at Site B. The NGRDI values ranged from -0.06 to 0.08 at Site A and -0.14 and 0.18 at Site B. Unlike the orthomosaics, the interpolation method generated a map over the whole flight area (Figure 4 and 7).

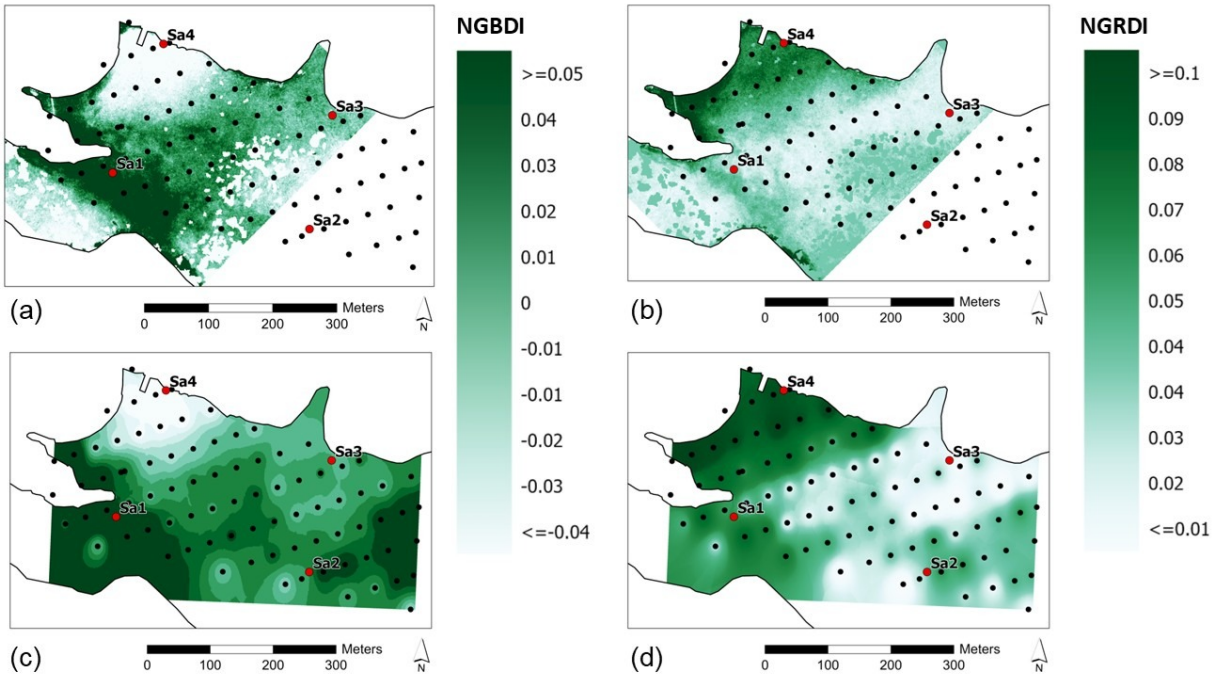

Figure 4. Site A orthomosaic derived (a) NGBDI, (b) NGRDI, and interpolated (c) NGBDI, (d) NGRDI from individual aerial photo central pixel values. Black points represent the photo locations and red points represent the sampling locations. North Carolina hydrography boundaries are found at https://www.nconemap.gov.

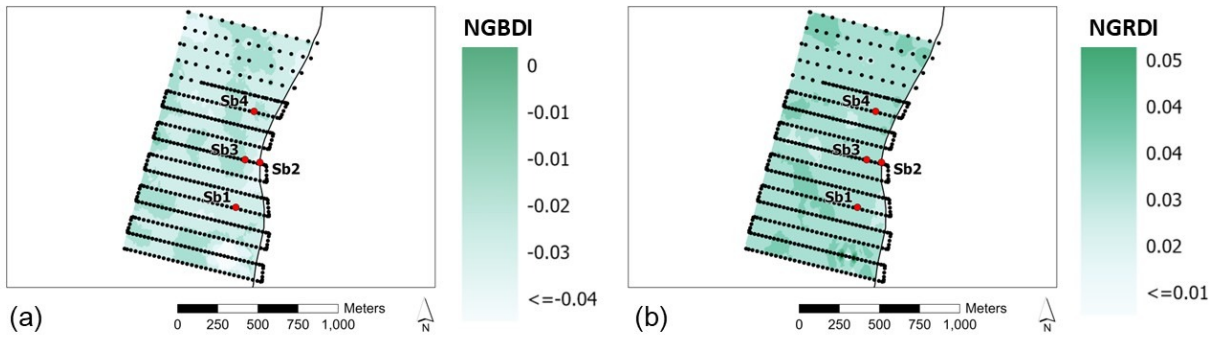

Figure 5. Site B interpolated (a) NGBDI, and (b) NGRDI from individual aerial photo central pixel values. Black points represent the photo locations and red points represent the sampling locations. North Carolina county boundaries are found at https://www.nconemap.gov/.

3.3 Water samples

In-vivo Chl-a fluorescence (proxy for phytoplankton biomass) varied at Site A by more than an order of magnitude (64.9 – 804 RFU) across all samplings (Figure A2). Collected surface water was dominated by *Microcystis* colonies (large and small) based on light microscopy, with very few cyanobacterial filaments (Figure 6A, B). In contrast, at Site B, *in-vivo* Chl-a fluorescence (proxy for phytoplankton biomass) showed less variation, ranging from 14.98 and 29.13 RFU across sampling locations (Table 3).

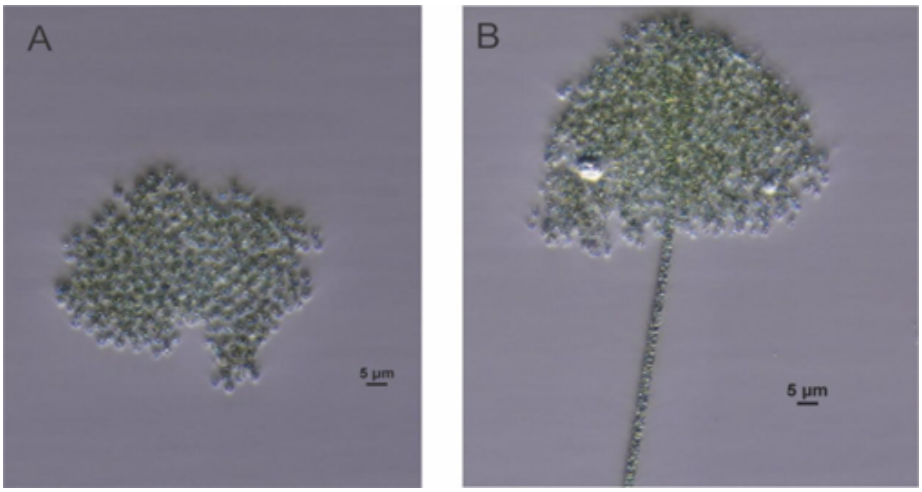

Figure 6. Micrographs of (A) an aggregation of *Microcystis* cells and (B) a *Microcystis* aggregate with an overlapping filamentous cyanobacterium.

Focusing on site A, *Microcystis* cells were present in all FCM samples based on Chl-a like fluorescence (Red-B) and phycocyanin-like fluorescence (Red-R) (Figure A1). On average, the *Microcystis* detected by FCM were 2.85 +/- 0.54 µm diameter (n = 11) (Table A1). We expect our concentration estimates to be lower than actual numbers given the possibility of small colonies (e.g. doublets, triplicates) being counted as single *Microcystis* cells by FCM. Larger *Microcystis* clusters were also detected but not enumerated as well as other small algae, e.g., *Synechococcus*-like cells and eukaryotic phytoplankton, (Figure A1) which are common in freshwater and

estuarine systems (96,97). Notably, *Microcystis* cell abundance and *in-vivo* Chl-a fluorescence increased in concert across sampling locations, which further points to *Microcystis* as the blooming taxa at Site A (Table A1).

Despite our limited water sample volume (~40 mL), cyanobacteria were detected by 16S rRNA PCR at nearly all Site A sampling locations. Surface water with the lowest *in-vivo* Chl-a fluorescence (~87 RFU) and 5.2x 10^3 *Microcystis*-like clusters per mL coincided with no PCR amplification of cyanobacterial 16S rRNA genes (Table A1). In contrast, *mcyA* genes were detectable by PCR in only one sample Sa4, which was also the richest in *Microcystis* cells.

Multiple microcystin congeners were detected from multiple particulate Site A samples, with MC-LR being most abundant (Tables A1, A2), illustrating the ability to detect cyanotoxins using high-resolution LC-MS/MS despite our small volume sampling approach. Notably though, toxins were not detectable in all samples and this was the case for samples with lowest *Microcystis* cell abundance and Chl-a fluorescence (Table A1). Highest MC concentrations were associated with highest concentrations of *Microcystis* and Chl-a fluorescence, which strongly points to active cyanotoxin production by the *Microcystis* bloom (Table A1).

3.4 Relationships between environmental variables

At Site A, the Spearman correlation coefficient (ρ) between spectral index values derived from the orthomosaics and their respective interpolation maps at 100 random sample points showed a strong positive association between NGDBI ($\rho > 0.78$) and NGRDI ($\rho > 0.94$). This analysis was not performed at Site B because of the inability to generate the orthomosaic over the water surface. At Site A and B, The Spearman correlation between the interpolations from the central pixel and the 9 and 25-cell averaged values also showed a strong positive association ($\rho > 0.94$). All models presented $P < 0.05$. The indices derived from the orthomosaics and interpolations at Sites A and B showed contrasting coefficient of determination values to predict *in-situ* Chl-a in the sample datasets (Tables 2 and 3). At Site A, NGBDI performed better at estimating Chl-a concentration (ortho-derived $R2 = 0.783$ and interpolated $R2 = 0.627$) than NGRDI (ortho-derived R2 = 0.084 and interpolated R2 = 0.019). Conversely, at Site B, NGRDI

performed better at estimating Chl-a concentration (interpolated $R2 = 0.898$) than NGBDI (interpolated $R2 = 0.452$).

Table 2. Site A Chl-a values from UAS sampling and the index values at the same location. Null values from areas where the orthomosaic was not generated.

Sample	*In vivo* Chl-a	Ortho NGBDI	IDW NGBDI	Ortho NGRDI	IDW NGRDI
Sa1	241.3	Null	0.0731	Null	-0.0385
Sa2	64.9	-0.0070	-0.0040	0.0480	0.0251
Sa3	87.45	0.0542	0.0600	-0.0371	-0.0474
Sa4	804.1	0.1180	0.1077	-0.0148	-0.0219
R^2		0.7830	0.6272	0.0844	0.0191

Table 3. Site B Chl-a values from UAS sampling and the index values at the same location.

Sample	*In vivo* Chl-a	IDW NGBDI	IDW NGRDI
Sb1	16.83	0.0245	-0.0159
Sb2	14.98	0.0161	-0.0186
Sb3	29.13	0.0315	-0.0111
Sb4	18.29	0.0318	-0.0149
R^2		0.4521	0.8976

4 Discussion

Here, we demonstrate using a low-cost UAS (< $1500) to collect and rapidly process images into a representative CyanoHAB distribution map for targeted water sample collection. Our method overcomes both the time to create an orthomosaic and the challenges of generating one over water. The previously reported inability to align aerial photos and, in turn, create a complete orthomosaic was the primary motivation for this work (35,37,38,53,60,61). It has been well documented that feature-based image matching in SfM software has difficulty with homogenous water surfaces (59,61). Additionally, the software can smooth or misrepresent the output (61). At our study sites, patchiness in the orthomosaics was expected and observed in areas with dense shoreline vegetation, along the flight area border, and over the homogenous water surface away from discernible features. Because of this, almost 40% of the photos were not aligned at Site A. This effect was especially pronounced at Site B, where more than 75% of the photos were not aligned. The generated orthomosaics were patchy over water and likely did not represent the surface conditions accurately. Some locations had duplicated features such as shorelines, cloud reflections, and floating debris.

While our methodology was initially developed to represent Chl-a distribution across water surfaces, its versatility extends to other applications, such as homogeneous agriculture fields, or snow-covered scenes, where orthomosaic generation is challenging (53). Moreover, processing imagery in the field is often time-consuming and requires high-end hardware. By bypassing the traditional orthomosaic generation workflow, we were able to rapidly produce maps that approximated CyanoHAB abundance for targeted sampling 20-100 times faster, with minimal computation power. This ability to process data quickly in environments with rapidly changing weather or moving water surfaces is of immense value for decision making (sampling, issuing public warnings) and maintaining time-series monitoring and capturing ephemeral events. For instance, UAS can be swiftly deployed to sample before or after adverse weather (98).

Using our approach, we were able to detect a cyanoHAB event, and subsequent analyses confirmed the presence of *Microcystis*, a genera of global public health and water quality

concern (1,99). Accordingly, identifying and predicting its presence, distribution, and production of cyanotoxins is of significant societal importance. Our UAS surveying and sampling methodology offers the potential to address these predictive challenges through rapid imaging and water sampling on finer temporal and spatial scales than what is available with typical 'grab' sampling. The targeted sampling approach provides the ability to identify algal 'hot spots' and probe them for toxin production, cell morphology (microscopy, FCM), and genetic composition. Overall, this flexible and non-disruptive sampling platform has diverse potential use as a bloom (*Microcystis* and beyond) interrogation tool. It is a platform that can enable rapid surveying and warning the public about potential/current 'toxin hot spots' or assessment of the evolution and composition of blooms on new temporal and spatial scales.

Our final sampling rig design offers a simple and effective means to collect surface water samples. The sampling rig was tested on large bodies of water in this study, but it could also be used on streams, ponds, or otherwise inaccessible or hazardous areas. While the rig was built for small consumer drones, it could be upscaled for larger commercial models. The final design choice to carry two 50 ml tubes was based on the carrying capacity, handling characteristics, wear on the UAS motors, and battery life. In tests, we collected up to 1 L with a DJI Phantom 4, but a single flight consumed more than half of the battery, it was difficult to control, and the motors were abnormally hot to the touch upon landing.

The spectral index maps produced from interpolation are visually aligned with the indices derived from the orthomosaic at Site A, confirmed by the random sample point value comparison. We could not perform this comparison at Site B because the orthomosaics could not be generated at that location. The comparison between spatial scales did not show a significant difference between the 1, 3x3, and 5x5 cell window resampling at either study site. This indicates that the central pixel adequately represents the water RGB values directly beneath the UAS for our purposes. The spectral indices presented a positive linear relationship with the chlorophyll-a values from the water samples, although each location performed better with a different index. The NGDBI showed a stronger relationship at Site A and NGRDI at Site B. These results align with visual interpretation of the maps and sufficiently capture the algae

distribution. More research is needed to evaluate if flight direction, water body type (estuarine vs. freshwater), season, and weather conditions impact the results. We did not test other indices that might perform differently.

While the interpolated index method discussed in this study may not be as accurate as an index derived from a well-generated orthomosaic, the results indicate effective mapping of algal biomass (CyanoHAB biomass) across a water body. The interpolated raster maps guide targeted water sampling in areas that would otherwise be in-mappable via the traditional methods. We envision this as a tool to capture environmental change in the short term from multiple locations. Additionally, this approach can provide cost savings for water managers and agencies while increasing safety for field personnel. For example, a single UAS pilot can collect imagery and samples from one shore location rather than a boat with multiple personnel.

5 Conclusion

Here we present a UAS-based method to rapidly estimate CyanoHAB variability and collect targeted water samples from inland and coastal waterbodies. The proposed process is fast and can estimate spectral index values representing chlorophyll over homogeneous water surfaces, a limitation of current workflows. The results of the interpolation method align well with orthomosaic-derived indices and UAS-collected water samples analyzed in the laboratory. Given that water quality and bloom conditions can be transitory, we feel our developed approach has the potential to bring monitoring, detection, and public warning of reduced water quality and potential health risks 'up to speed' with changes in aquatic systems.

Funding: The research at Waterville Reservoir was funded by Duke Energy.

Acknowledgments: Thanks to Attollo LLC, Theorem Geo, and Duke Energy for providing personnel, resources, and coordination for the harmful algal bloom UAS pilot project at Waterville Reservoir.

Appendix

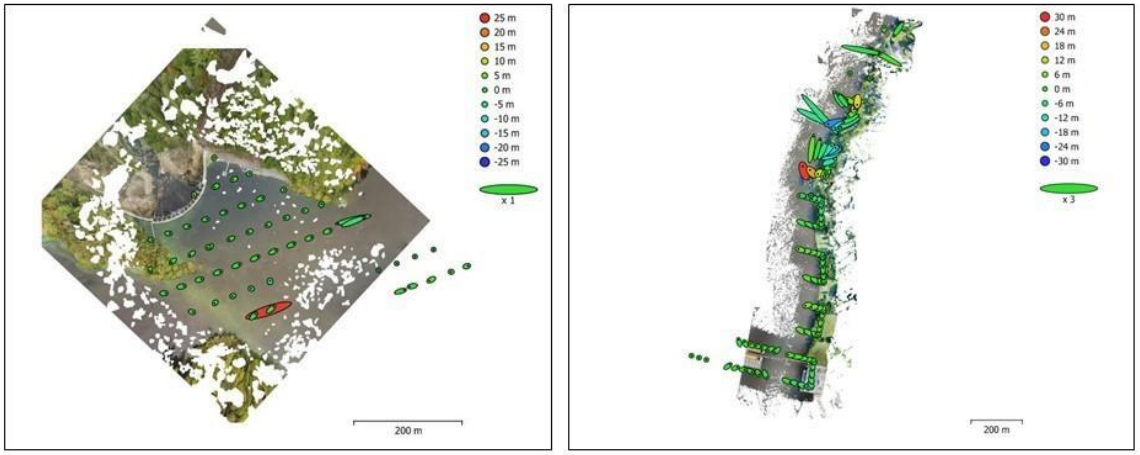

Figure A1. Orthomosaics from Metashape processing report with camera locations and error estimates for the (a) Site A and (b) Site B flights. Estimated camera locations are marked with black points. Z error is represented by ellipse color and X and Y errors are represented by ellipse shape.

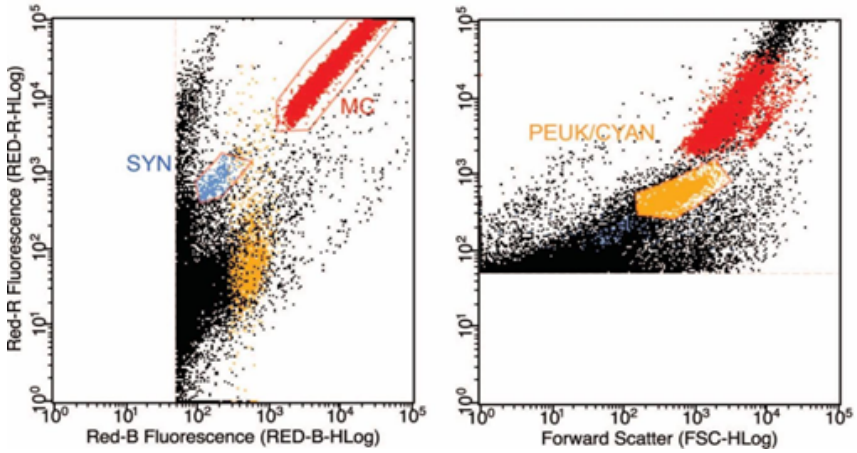

Figure A2. Example FCM data from Site A sampling. The gating used to enumerate populations are shown, with consistent color coding across plots. *Microcystis*-like cells (MC) are in red. Smaller phycocyanin-rich *Synechococcus*-like cells (SYN) are in blue, and putative picoeukaryotic algae or larger unicellular cyanobacteria lacking phycoerythrin (PEUK/CYAN) are in orange. Larger *Microcystis*-like cells or clusters are evident in the top right of the right panel but were not quantified.

Table A1. Measured parameters from Site A surface water samples. ++ = strong PCR amplification; + = weak PCR amplification. MC= Microcystin. ND = not detected by LC-MS/MS.

Sample ID	*In vivo* Chl a Fluorescence (RFU)	*Microcystis* (cells/mL)	DNA Concentration (ng/µL)	Cyano 16S rRNA positive?	*mcyA* positive?	Total MC per L (µg/L)
Sa1	241.3	3.2E+04	0.338	+		0.386
Sa2	64.9	1.6E+04	0.18	+		0.209
Sa3	87.45	5.2E+03	0.374			ND
Sa4	804.1	3.3E+05	45.2	++	+	3.589
Sa5	75.93	2.7E+03	0.282			ND
Sa6	348.8	2.3E+05	2.64	++		1.064
Sa7	71.96	4.1E+03	0.112			ND
Sa8	69.22	2.7E+03	0.178			ND
Sa9	82.94	9.5E+03	0.216	+		0.131
Sa10	111.7	3.1E+04	0.49			0.528
Sa11	98.47	9.6E+03	0.492	+		ND

Table A2. Concentrations of total Microcystin and congener forms (with different amino acid side groups) in the particulate phase of Site A surface water samples. MC = Microcystin.

Sample ID	Total MC (pg)	Total MC per L (ng/L)	Total MC per L (µg/L)	MC-LA (ng/L)	MC-LR (ng/L)	MC-LY (ng/L)	MC-YR (ng/L)	D-Asp-MC-LR (ng/L)	MC-LF (ng/L)	MC-LW (ng/L)	MC-WR (ng/L)
Sa1	3.86E+03	3.86E+02	3.86E-01	<0.56	3.86E+02	<0.8	<0.85	<0.25	<0.24	<0.14	<0.61
Sa2	2.09E+03	2.09E+02	2.09E-01	<0.56	2.09E+02	<0.8	<0.85	<0.25	<0.24	<0.14	<0.61
Sa3	<4.08E+02	<4.09E+01	<4.09E-02	<0.56	<0.64	<0.8	<0.85	<0.25	<0.24	<0.14	<0.61
Sa4	3.59E+04	3.59E+03	3.59E+00	<0.56	2.29E+03	2.92E+02	2.56E+02	<0.25	2.01E+02	2.94E+02	2.57E+02
Sa5	<4.08E+02	<4.09E+01	<4.09E-02	<0.56	<0.64	<0.8	<0.85	<0.25	<0.24	<0.14	<0.61
Sa6	1.06E+04	1.06E+03	1.06E+00	<0.56	7.81E+02	<0.8	1.89E+02	<0.25	<0.24	9.42E+01	<0.61
Sa7	<4.08E+02	<4.09E+01	<4.09E-02	<0.56	<0.64	<0.8	<0.85	<0.25	<0.24	<0.14	<0.61
Sa8	<4.08E+02	<4.09E+01	<4.09E-02	<0.56	<0.64	<0.8	<0.85	<0.25	<0.24	<0.14	<0.61
Sa9	1.31E+03	1.31E+02	1.31E-01	<0.56	4.02E+01	<0.8	<0.85	<0.25	<0.24	<0.14	9.05E+01
Sa10	5.28E+03	5.28E+02	5.28E-01	<0.56	3.42E+02	<0.8	1.11E+02	<0.25	<0.24	<0.14	7.53E+01
Sa11	<4.08E+02	<4.09E+01	<4.09E-02	<0.56	<0.64	<0.8	<0.85	<0.25	<0.24	<0.14	<0.61

References

1. Paerl HW, Otten TG. Harmful Cyanobacterial Blooms: Causes, Consequences, and Controls. Microbial ecology. 2013;65(4):995–1010.

2. Dvořáková-Hladká J. Fogg, ge, stewart, wdp, Fay, p., Walsby, ae: The blue-green algae: Academic Press, London-New York 1973, 459 pp., 8.50£. 1974;

3. Reynolds C. The ecology of freshwater phytoplankton. Vol. 384. Cambridge University Press; 1984.

4. Tomas CR. Identifying marine phytoplankton. Elsevier; 1997.

5. Plaas HE, Paerl RW, Baumann K, Karl C, Popendorf KJ, Barnard MA, et al. Harmful cyanobacterial aerosolization dynamics in the airshed of a eutrophic estuary. The Science of the total environment. 2022;852(Journal Article):158383–158383.

6. Paerl HW, Otten TG, Kudela R. Mitigating the Expansion of Harmful Algal Blooms Across the Freshwater-to-Marine Continuum. Environmental science & technology. 2018;52(10):5519–29.

7. Sotton B, Guillard J, Anneville O, Maréchal M, Savichtcheva O, Domaizon I. Trophic transfer of microcystins through the lake pelagic food web: Evidence for the role of zooplankton as a vector in fish contamination. Science of the Total Environment. 2014;466:152–63.

8. Flores NM, Miller TR, Stockwell JD. A global analysis of the relationship between concentrations of microcystins in water and fish. Frontiers in Marine Science. 2018;5:30.

9. Wolf D, Klaiber HA. Bloom and bust: Toxic algae's impact on nearby property values. Ecological economics. 2017;135:209–21.

10. Paerl HW, Fulton RS, Moisander PH, Dyble J. Harmful freshwater algal blooms, with an emphasis on cyanobacteria. The scientific world journal. 2001;1:76.

11. Elliott JA. Is the future blue-green? A review of the current model predictions of how climate change could affect pelagic freshwater cyanobacteria. Water research. 2012;46(5):1364–71.

12. Huisman J, Codd GA, Paerl HW, Ibelings BW, Verspagen JM, Visser PM. Cyanobacterial blooms. Nature Reviews Microbiology. 2018;16(8):471–83.

13. Bullerjahn GS, McKay RM, Davis TW, Baker DB, Boyer GL, D'Anglada LV, et al. Global solutions to regional problems: Collecting global expertise to address the problem of harmful cyanobacterial blooms. A Lake Erie case study. Harmful algae. 2016;54:223–38.

14. Stumpf RP, Davis TW, Wynne TT, Graham JL, Loftin KA, Johengen TH, et al. Challenges for mapping cyanotoxin patterns from remote sensing of cyanobacteria. Harmful algae. 2016;54:160–73.

15. Seegers BN, Werdell PJ, Vandermeulen RA, Salls W, Stumpf RP, Schaeffer BA, et al. Satellites for long-term monitoring of inland U.S. lakes: The MERIS time series and application for chlorophyll-a. Remote sensing of environment. 2021;266(Journal Article):112685–14.

16. North Carolina Division of Water Resources. Intensive Survey Branch Standard Operating Procedures Manual: Physical and Chemical Monitoring; Report Prepared for North Carolina Division of Water Resources. 2013; Available from: https://files.nc.gov/ncdeq/Water%20Quality/Environmental%20Sciences/ECO/algae/Algal-Bloom-Field-Collecton-Method-FINAL-6.15.20.pdf

17. Koparan C, Koc AB, Privette CV, Sawyer CB. In Situ Water Quality Measurements Using an Unmanned Aerial Vehicle (UAV) System. Water. 2018;10(3).

18. Koparan C, Privette CV, Sawyer CB. Autonomous In Situ Measurements of Noncontaminant Water Quality Indicators and Sample Collection with a UAV. Water. 2019;11(3):604.

19. World Health Organization. Cyanobacterial toxins: microcystins [Internet]. Geneva: World Health Organization; 2020. Available from: https://apps.who.int/iris/handle/10665/338066

20. Ore JP, Elbaum S, Burgin A, Zhao B, Detweiler C. Autonomous Aerial Water Sampling. In: Mejias L, Corke P, Roberts J, editors. Field and Service Robotics: Results of the 9th International Conference [Internet]. Cham: Springer International Publishing; 2015. p. 137–51. Available from: https://doi.org/10.1007/978-3-319-07488-7_10

21. Graham CT, O'Connor I, Broderick L, Broderick M, Jensen O, Lally HT. Drones can reliably, accurately and with high levels of precision, collect large volume water samples and physio-chemical data from lakes. Science of The Total Environment. 2022 June 10;824:153875.

22. Song K, Brewer A, Ahmadian S, Shankar A, Detweiler C, Burgin AJ. Using unmanned aerial vehicles to sample aquatic ecosystems. Limnology and oceanography, methods. 2017;15(12):1021–30.

23. Benson J, Hanlon R, Seifried T, Baloh P, Powers C, Grothe H, et al. Microorganisms Collected from the Surface of Freshwater Lakes Using a Drone Water Sampling System (DOWSE). Water (Basel). 2019;11(1):157.

24. Terada A, Morita Y, Hashimoto T, Mori T, Ohba T, Yaguchi M, et al. Water sampling using a drone at Yugama crater lake, Kusatsu-Shirane volcano, Japan. Earth, Planets and Space. 2018 Apr 19;70(1):64.

25. Horricks RA, Bannister C, Lewis-McCrea LM, Hicks J, Watson K, Reid GK. Comparison of drone and vessel-based collection of microbiological water samples in marine environments. Environmental Monitoring and Assessment. 2022 May 20;194(6):439.

26. Koparan C, Koc A, Privette C, Sawyer C, Sharp J. Evaluation of a UAV-Assisted Autonomous Water Sampling. Water (Basel). 2018;10(5):655.

27. Lally HT, O'Connor I, Jensen OP, Graham CT. Can drones be used to conduct water sampling in aquatic environments? A review. Science of The Total Environment. 2019 June 20;670:569–75.

28. Hodgson ME, Vitzilaios NI, Myrick ML, Richardson TL, Duggan M, Sanim KRI, et al. Mission Planning for Low Altitude Aerial Drones during Water Sampling. Drones. 2022;6(8).

29. Khan RM, Salehi B, Mahdianpari M, Mohammadimanesh F, Mountrakis G, Quackenbush LJ. A Meta-Analysis on Harmful Algal Bloom (HAB) Detection and Monitoring: A Remote Sensing Perspective. Remote Sensing. 2021;13(21).

30. Caballero I, Fernández R, Escalante OM, Mamán L, Navarro G. New capabilities of Sentinel-2A/B satellites combined with in situ data for monitoring small harmful algal blooms in complex coastal waters. Scientific reports. 2020;10(1):8743.

31. Schaeffer BA, Bailey SW, Conmy RN, Galvin M, Ignatius AR, Johnston JM, et al. Mobile device application for monitoring cyanobacteria harmful algal blooms using Sentinel-3 satellite Ocean and Land Colour Instruments. Environmental modelling & software : with environment data news. 2018;109(Journal Article):93–103.

32. Sharp SL, Forrest AL, Bouma-Gregson K, Jin Y, Cortés A, Schladow SG. Quantifying Scales of Spatial Variability of Cyanobacteria in a Large, Eutrophic Lake Using

Multiplatform Remote Sensing Tools. Frontiers in Environmental Science [Internet]. 2021;9. Available from: https://www.frontiersin.org/articles/10.3389/fenvs.2021.612934

33. Coffer MM, Schaeffer BA, Darling JA, Urquhart EA, Salls WB. Quantifying national and regional cyanobacterial occurrence in US lakes using satellite remote sensing. Ecological indicators. 2020;111(Journal Article):105976.

34. Schaeffer BA, Myer MH. Resolvable estuaries for satellite derived water quality within the continental United States. Remote sensing letters. 2020;11(6):535–44.

35. Wu D, Li R, Zhang F, Liu J. A review on drone-based harmful algae blooms monitoring. Environmental Monitoring and Assessment. 2019 Mar 9;191(4):211.

36. Sozzi M, Kayad A, Gobbo S, Cogato A, Sartori L, Marinello F. Economic Comparison of Satellite, Plane and UAV-Acquired NDVI Images for Site-Specific Nitrogen Application: Observations from Italy. Agronomy (Basel). 2021;11(11):2098.

37. Kislik C, Dronova I, Kelly M. UAVs in Support of Algal Bloom Research: A Review of Current Applications and Future Opportunities. Drones. 2018;2(4).

38. Silvarrey Barruffa A, Pardo Á, Faggian R, Sposito V. Monitoring cyanobacterial harmful algal blooms by unmanned aerial vehicles in aquatic ecosystems. Environ Sci: Water Res Technol. 2021;7(3):573–83.

39. Cobelo I, Machado KB, David ACM, Carvalho P, Ferreira ME, Nabout JC. Unmanned aerial vehicles and low-cost sensor as tools for monitoring freshwater chlorophyll-a in mesocosms with different trophic state. International Journal of Environmental Science and Technology. 2022;1–12.

40. Maravilla RMG, Quinalayo JP, Blanco AC, Candido CG, Gubatanga EV, Ticman KDV. ESTIMATION OF CHLOROPHYLL-A CONCENTRATION IN SAMPALOC LAKE USING UAS MULTISPECTRAL REMOTE SENSING AND REGRESSION ANALYSIS. International archives of the photogrammetry, remote sensing and spatial information sciences. 2019;XLII-4/W19(Journal Article):297–303.

41. Larrinaga AR, Brotons L. Greenness indices from a low-cost UAV imagery as tools for monitoring post-fire forest recovery. Drones. 2019;3(1):6.

42. Richardson AD, Jenkins JP, Braswell BH, Hollinger DY, Ollinger SV, Smith ML. Use of Digital Webcam Images to Track Spring Green-Up in a Deciduous Broadleaf Forest. Oecologia. 2007;152(2):323–34.

43. Woebbecke DM, Meyer GE, Von Bargen K, Mortensen DA. Color indices for weed identification under various soil, residue, and lighting conditions. Transactions of the ASAE. 1995;38(1):259–69.

44. Xu F, Gao Z, Jiang X, Shang W, Ning J, Song D, et al. A UAV and S2A data-based estimation of the initial biomass of green algae in the South Yellow Sea. Marine pollution bulletin. 2018;128:408–14.

45. Sonnentag O, Hufkens K, Teshera-Sterne C, Young AM, Friedl M, Braswell BH, et al. Digital repeat photography for phenological research in forest ecosystems. Agricultural and forest meteorology. 2012;152(Journal Article):159–77.

46. Motohka T, Nasahara KN, Oguma H, Tsuchida S. Applicability of green-red vegetation index for remote sensing of vegetation phenology. Remote Sensing. 2010;2(10):2369–87.

47. Rouse JW, Haas RH, Schell JA, Deering DW. Monitoring vegetation systems in the Great Plains with ERTS. NASA special publication. 1974;351(1974):309.

48. Tucker CJ. Red and photographic infrared linear combinations for monitoring vegetation. Remote sensing of Environment. 1979;8(2):127–50.

49. Gitelson AA, Kaufman YJ, Stark R, Rundquist D. Novel algorithms for remote estimation of vegetation fraction. Remote sensing of environment. 2002;80(1):76–87.

50. Louhaichi M, Borman MM, Johnson DE. Spatially Located Platform and Aerial Photography for Documentation of Grazing Impacts on Wheat. null. 2001 Mar 1;16(1):65–70.

51. Xiaoqin W, Miaomiao W, Shaoqiang W, Yundong W. Extraction of vegetation information from visible unmanned aerial vehicle images. Transactions of the Chinese Society of Agricultural Engineering. 2015;31(5).

52. Shiraishi H. New index for estimation of chlorophyll-a concentration in water with RGB value. Int J Eng Technol. 2018;18(6):10–6.

53. Jeziorska J. UAS for Wetland Mapping and Hydrological Modeling. Remote Sensing. 2019;11(17).

54. Johansen K, Dunne AF, Tu YH, Almashharawi S, Jones BH, McCabe MF. Dye tracing and concentration mapping in coastal waters using unmanned aerial vehicles. Scientific Reports. 2022 Jan 21;12(1):1141.

55. Griffiths D, Burningham H. Comparison of pre- and self-calibrated camera calibration models for UAS-derived nadir imagery for a SfM application. Progress in Physical Geography: Earth and Environment. 2018 July 24;43:030913331878896.

56. Carbonneau PE, Dietrich JT. Cost-effective non-metric photogrammetry from consumer-grade sUAS: implications for direct georeferencing of structure from motion photogrammetry. Earth Surface Processes and Landforms. 2017 Mar 15;42(3):473–86.

57. James MR, Antoniazza G, Robson S, Lane SN. Mitigating systematic error in topographic models for geomorphic change detection: accuracy, precision and considerations beyond off-nadir imagery. Earth Surface Processes and Landforms. 2020 Aug 1;45(10):2251–71.

58. Guan S, Sirianni H, Wang G, Zhu Z. sUAS Monitoring of Coastal Environments: A Review of Best Practices from Field to Lab. Drones (Basel). 2022;6(6):142.

59. Hashemi-Beni L, Jones J, Thompson G, Johnson C, Gebrehiwot A. Challenges and Opportunities for UAV-Based Digital Elevation Model Generation for Flood-Risk Management: A Case of Princeville, North Carolina. Sensors [Internet]. 2018;18(11). Available from: https://www.mdpi.com/1424-8220/18/11/3843

60. Gray PC, Windle AE, Dale J, Savelyev IB, Johnson ZI, Silsbe GM, et al. Robust ocean color from drones: Viewing geometry, sky reflection removal, uncertainty analysis, and a survey of the Gulf Stream front. Limnology and Oceanography: Methods. 2022 Oct 1;20(10):656–73.

61. Bogolin AP, Davis DR, Kline RJ, Rahman AF. A drone-based survey for large, basking freshwater turtle species. PLOS ONE. 2021 Oct 27;16(10):e0257720.

62. Lee JS, Baek JY, Jung D, Shim JS, Lim HS, Jo YH. Estimate of Coastal Water Depth Based on Aerial Photographs Using a Low-Altitude Remote Sensing System. Ocean Science Journal. 2019 Sept 1;54(3):349–62.

63. Román A, Heredia S, Windle AE, Tovar-Sánchez A, Navarro G. Enhancing Georeferencing and Mosaicking Techniques over Water Surfaces with High-Resolution Unmanned Aerial Vehicle (UAV) Imagery. Remote Sensing. 2024;16(2):290.

64. Barrett M. Algal bloom, toxins found in Waterville Lake. The Greenville News. 2015;

65. Sen A. Algae bloom threatens public at Fontana, Waterville lakes. Asheville Citizen - Times. 2017;

66. Haywood County Emergency Services. Potentially harmful algal blooms found in Waterville Lake. Mountain Xpress [Internet]. 2021; Available from: https://mountainx.com/blogwire/potentially-harmful-algal-blooms-in-waterville-lake/

67. Paerl HW, Ustach JF. Blue-green algal scums: An explanation for their occurrence during freshwater blooms1. Limnology and Oceanography. 1982 Mar 1;27(2):212–7.

68. Walters Hydroelectric Plant [Internet]. Duke Energy; 2019 [cited 2019 June 10]. Available from: https://www.duke-energy.com/our-company/about-us/power-plants

69. Coombs JA, Wilson L, Tracy B, Harrison V. Pigeon River revival. Wildlife in North Carolina. 2004;68(12):26–9.

70. North Carolina Department of Environment and Natural Resources, North Carolina. Environmental Management Commission, North Carolina. Division of Water Quality.Planning Section. Chowan River Basin Water Resources Plan [Internet]. Raleigh, N.C: NC Department of Environment & Natural Resources, Division of Water Quality /Planning; 2021 [cited 2022 Mar 9]. Available from:

https://deq.nc.gov/about/divisions/water-resources/water-planning/basin-planning/river-basin-plans/chowan/chowan-river-basin-water-resources-plan

71. Technical specifications ANAFI Thermal [Internet]. Parrot; 2019. Available from: https://www.parrot.com/us/drones/anafi-thermal/technical-specifications

72. U-blox UBX-M8030 Product Summary [Internet]. U-blox; 2019. Available from: https://www.u-blox.com/en/product/ubx-m8030-series

73. Pix4dcapture [Internet]. Pix4d; 2018. Available from: https://www.pix4d.com/product/pix4dcapture

74. Phantom 4 Pro Specs [Internet]. DJI; 2019. Available from: https://www.dji.com/uk/phantom-4-pro/info?redirect_info=true#specs

75. DroneDeploy. DroneDeploy Flight App. V.2.73.0 [Internet]. San Francisco, California; 2021 [cited 2018 June 10]. Available from: https://www.dronedeploy.com

76. Agisoft. Agisoft Metashape V.1.7.5 [Internet]. St. Petersburg, Russia; 2021. Available from: https://www.agisoft.com/

77. Agisoft. Agisoft Metashape User Manual Version 1.7.5 [Internet]. Agisoft; 2021. Available from: https://www.agisoft.com/

78. ESRI. ArcGIS Pro V.2.9.0 [Internet]. Redlands, California; 2021 [cited 2021 Sept 20]. Available from: https://pro.arcgis.com

79. Sunoj S, Hammed A, Igathinathane C, Eshkabilov S, Simsek H. Identification, quantification, and growth profiling of eight different microalgae species using image analysis. Algal Research. 2021;60:102487.

80. Jiang X, Gao M, Gao Z. A novel index to detect green-tide using UAV-based RGB imagery. Estuarine, Coastal and Shelf Science. 2020;245:106943.

81. U.S. Geological Survey. National Hydrography Dataset (NHD) [Internet]. 2021 [cited 2021 May 18]. Available from: https://prd-tnm.s3.amazonaws.com/StagedProducts/Hydrography/NHD/State/GDB/NHD_H_North_Carolina_State_GDB.zip

82. Clark A. Python Pillow [Internet]. 2022 [cited 2021 Sept 20]. Available from: https://python-pillow.org/

83. Williams J. gpsphoto 2.2.3 [Internet]. 2022 [cited 2021 Sept 20]. Available from: https://pypi.org/project/gpsphoto/

84. FreeFlight 6 [Internet]. Parrot; 2019. Available from: https://support.parrot.com/us/support/products/anafi/

85. DJI. DJI GO. V.4.3.37 [Internet]. Shenzhen, China; 2021. Available from: https://www.dji.com/goapp

86. Paerl RW, Venezia RE, Sanchez JJ, Paerl HW. Picophytoplankton dynamics in a large temperate estuary and impacts of extreme storm events. Scientific reports. 2020;10(1):22026–15.

87. Gaston CJ, Royer HM, Leibensperger RJI, Maizel D, Lanpher KB, Solo-Gabriele H, et al. Filtration Efficiency of Air Conditioner Filters and Face Masks to Limit Exposure to Aerosolized Algal Toxins. Aerosol and air quality research. 2021;21(8):210016.

88. Liu H, Jing H, Wong THC, Chen B. Co-occurrence of phycocyanin- and phycoerythrin-rich Synechococcus in subtropical estuarine and coastal waters of Hong Kong. Environmental microbiology reports. 2014;6(1):90–9.

89. Nubel U, Garcia-Pichel F, Muyzer G. PCR primers to amplify 16S rRNA genes from cyanobacteria. Applied and Environmental Microbiology. 1997;63(8):3327–32.

90. Hisbergues M, Christiansen G, Rouhiainen L, Sivonen K, Börner T. PCR-based identification of microcystin-producing genotypes of different cyanobacterial genera. Archives of microbiology. 2003;180(6):402–10.

91. QGIS. QGIS Geographic Information System [Internet]. 2022 [cited 2021 Sept 20]. Available from: https://qgis.org

92. Harris CR, Millman KJ, van der Walt SJ, Gommers R, Virtanen P, Cournapeau D, et al. Array programming with NumPy. Nature (London). 2020;585(7825):357–62.

93. ImportPhotos: a QGIS plugin to visualise geotagged photos. v.2.2. [Internet]. [cited 2019 July 16]. Available from: https://mariosmsk.com/2019/07/02/qgis-plugin-importphotos/

94. Virtanen P, Gommers R, Oliphant TE, Haberland M, Reddy T, Cournapeau D, et al. SciPy 1.0: fundamental algorithms for scientific computing in Python. Nature methods. 2020;17(3):261–72.

95. NC OneMap. Latest Orthoimagery [Internet]. 2020 [cited 2020 Jan 19]. Available from: https://services.nconemap.gov/secure/rest/services/Imagery/Orthoimagery_Latest/ImageServer

96. Stockner JG, Antia NJ. Algal Picoplankton from Marine and Freshwater Ecosystems: A Multidisciplinary Perspective. Canadian journal of fisheries and aquatic sciences. 1986;43(12):2472–503.

97. Callieri C. Picophytoplankton in Freshwater Ecosystems: The Importance of Small-Sized Phototrophs. Callieri C (comp), editor. Freshwater reviews. 2008;1(1):1–28.

98. Vélez-Nicolás M, García-López S, Barbero L, Ruiz-Ortiz V, Sánchez-Bellón Á. Applications of Unmanned Aerial Systems (UASs) in Hydrology: A Review. Remote Sensing. 2021;13(7).

99. Harke MJ, Steffen MM, Gobler CJ, Otten TG, Wilhelm SW, Wood SA, et al. A review of the global ecology, genomics, and biogeography of the toxic cyanobacterium, Microcystis spp. Harmful algae. 2016;54:4–20.